Enhancing Tropospheric Zenith Wet Delay Interpolation With Gaussian Process Regression

Xuejie Hou, Yiping Jiang, and Xingqun Zhan, *Senior Member, IEEE*

***Abstract*— Accurate estimation of zenith wet delay (ZWD) plays a vital role in enhancing precision and reducing the convergence time of Global Navigation Satellite System (GNSS) positioning. However, ZWD's spatial distribution is highly complex and variable due to its dependence on atmospheric water vapor, which introduces significant challenges in estimation. Traditional methods, such as ordinary kriging, assume second-order stationarity and may fail with highly dispersed datasets or sparse networks. To overcome these limitations, this study proposes Gaussian process regression (GPR) as a promising alternative. GPR offers greater adaptability and flexibility in modeling complex spatial structures without relying on strict stationarity assumptions. To evaluate GPR's performance, we utilized 2022 ZWD data from 39 reference stations in North America and 19 reference stations in Hong Kong. Our comparative analyses reveal that in North America, GPR improves the estimation accuracy by up to 2.9 cm compared to ordinary kriging while also reducing computation time. In Hong Kong, while GPR and ordinary kriging achieve similar fitting accuracy, ordinary kriging occasionally exhibits rapid convergence to a mean level, indicating an oversimplification of spatial structures. In contrast, GPR consistently maintains its performance without such issues. These findings highlight the adaptability and efficiency of GPR in diverse geographical settings, making it a robust choice for ZWD estimation.**

***Index Terms*— Computational efficiency, fitting accuracy, Gaussian process regression (GPR), ordinary kriging, zenith wet delay (ZWD).**

I. Introduction

SITUATED as the Earth's lowest atmospheric layer, the troposphere is known to introduce signal distortions in Global Navigation Satellite System (GNSS), predominantly quantified by the tropospheric zenith total delay (ZTD). ZTD is composed of two primary elements: the zenith hydrostatic delay (ZHD) and the zenith wet delay (ZWD) [1]. ZHD, constituting approximately 90% of ZTD, can reach extents of 2–3 m in the zenith direction [2]. Conversely, ZWD varies based on atmospheric water vapor content, spanning from a few centimeters in arid regions to about 35 cm in humid areas [3]. Despite ZHD's larger absolute value, attributed to relatively consistent atmospheric pressure profiles, it is relatively straightforward to model and compute [4]. On the other hand, the ZWD, with its dependence on the highly variable water vapor content, presents more significant challenges.

The variability in ZWD poses a significant challenge in GNSS positioning techniques, particularly in precise point positioning (PPP) and PPP real-time kinematic (PPP-RTK). These advanced technologies aim to achieve high-accuracy positioning at the centimeter level or better in real time. To enhance the performance of PPP and PPP-RTK, ZWD values obtained through interpolation methods can be utilized as a priori values, aiding in ambiguity resolution and improving the convergence speed of PPP [5]. Furthermore, to augment PPP-RTK technology, ZWD values derived from GNSS network services can be interpolated to estimate user-specific ZWD values, which can then be broadcast to GNSS rovers [6]. Moreover, ZWD is directly correlated with the precipitable water vapor (PWV) in the atmosphere, making its precise estimation critical for both enhancing GNSS positioning accuracy and improving the reliability of meteorological forecasts [7], [8], [9]. Precise estimation of ZWD is crucial for improving GNSS positioning accuracy and can also contribute to the reliability of meteorological forecasts.

Over the years, various methods and models have been proposed to address the ZWD error in GNSS. These approaches can be broadly categorized into empirical models and interpolation-based methods. Empirical models rely on atmospheric parameters such as temperature, pressure, and humidity to compute the delay [10]. Some well-known examples include the Saastamoinen [11], Hopfield models [12], and uniform atmosphere tropospheric error model [13].

In recent years, with the rapid development of artificial intelligence (AI) technology, various AI-based methods have emerged as a subset of empirical models, demonstrating promising performance in ZWD estimation. These methods use similar input parameters as traditional empirical models but leverage machine learning techniques to capture complex relationships. For instance, Ding et al. [14] developed a global model outperforming empirical model by neural networks, while Yang et al. [15], Mohammed [16], and Selbesoglu [17] have all reported successful applications

Received 11 July 2024; revised 12 September 2024; accepted 6 October 2024. Date of publication 17 October 2024; date of current version 14 November 2024. This work was supported by the Research Grants Council of Hong Kong Special Administrative Region, China, under Project 25202520 and Project 15214523. *(Corresponding author: Yiping Jiang.)*

Xuejie Hou and Yiping Jiang are with the Department of Aeronautical and Aviation Engineering, The Hong Kong Polytechnic University, Hong Kong, China (e-mail: 22038337r@connect.polyu.hk; yiping.jiang@polyu.edu.hk).

Xingqun Zhan is with the School of Aeronautics and Astronautics, Shanghai Jiao Tong University, Minhang, Shanghai 200240, China (e-mail: xqzhan@sjtu.edu.cn).

Digital Object Identifier 10.1109/TGRS.2024.3482415

of artificial neural networks in regional ZWD estimation. More recently, Crocetti et al. [18] presented a global, spatially explicit ZWD model using the extreme gradient boosting (XGBoost) algorithm. Their model takes meteorological variables, geographical location, and time as inputs and can predict ZWD anywhere on Earth with high accuracy.

These models have proven reliable; however, they often rely on the very data they aim to correct, as atmospheric parameters are frequently derived from ZWD analysis. In contrast, interpolation approaches estimate a user's ZWD by leveraging known ZWD values and positions of reference stations, establishing a spatial relationship between these reference points and the user's location. Traditional interpolation methods consider ZWD error as a common spatial error, which can be mitigated through techniques such as the distance-based linear interpolation model (DIM) [19], linear interpolation model (LIM) [20], linear combination model (LCM) [21], and linear surface model (LSM) [5]. These linear-model variants utilize various combinations of known data points to estimate tropospheric delay, primarily modeling the distance-dependent biases between reference stations and user receivers. Despite their simplicity and widespread use in real-time kinematic (RTK) and PPP-RTK [22], [23], these methods may have limited accuracy in areas with complex tropospheric variations.

To address the limitations of linear interpolation methods, ordinary kriging has emerged as a viable alternative for ZWD estimation. This geostatistical technique takes into account both the distance and the spatial correlation structure of the data, positing that values at proximate locations are more similar than those at distant ones. By employing a variogram or semivariogram to quantify the decline in spatial correlation as the distance between points increases, ordinary kriging can effectively capture the spatial dependence of ZWD. The validity of using ordinary kriging for ZWD estimation has been demonstrated in various studies. Ma et al. [2] showed that ordinary kriging is suitable across different seasons and network types. AI-Shaery et al. [24] compared three semivariogram models—spherical, exponential, and Gaussian—and concluded that their accuracies are comparable. Kim and Kee [25] applied ordinary kriging with a specific variogram model tailored for rainy conditions to improve the positioning of autonomous ground vehicles during rain.

However, ordinary kriging is based on certain stringent assumptions, particularly the stationarity assumption, which posits that statistical properties are consistent across space [26]. Some specific weather conditions may lead to the violation of the spatial stationarity assumption for tropospheric wet delay. For instance, when there are significant changes in weather conditions or precipitation occurs, the humidity distribution in the atmosphere may undergo drastic changes. This can result in the tropospheric wet delay no longer satisfying spatial stationarity between precipitation and nonprecipitation areas, as the difference in humidity between these areas could be substantial.

In contrast, Gaussian process regression (GPR) does not require the assumption of spatial stationarity. GPR is a nonparametric, probabilistic model that infers spatial relationships through the use of kernels, which are functions that measure the similarity between data points [27]. By selecting appropriate kernels, GPR can flexibly capture complex spatial patterns and accommodate varying conditions without the need for the statistical properties to be consistent across space. This makes GPR particularly suitable for scenarios with various weather conditions or heterogeneous environments.

Moreover, Christianson et al. [26] noted that ordinary kriging and its requirement for variogram inspection are inherently hands-on processes. A significant advantage of machine learning algorithms, such as GPR, over ordinary kriging is their capacity for automating kernel inference. This automation eliminates the need for manual kernel selection and tuning, processes that are often subjective and time-consuming, thus paving the way for more efficient and objective analysis [28], [29]. Table I summarizes the key methods and models discussed in the literature for addressing ZWD error in GNSS, along with their key assumptions and limitations.

The main objectives of this article are as follows. First, we utilize the GPR algorithm to interpolate ZWD values in North America and Hong Kong and compare it with ordinary kriging in terms of both accuracy and computational efficiency. Our findings suggest that ordinary kriging may not be suitable for data distributions that do not meet the stationarity assumption, such as those observed in certain regions of North America and under highly dispersed datasets. Finally, we identify other factors affecting ZWD estimation, including the correlation coefficient (CC) of input information and geographical considerations.

The structure of this article is organized as follows. Section I provides an introduction to the background and objectives of the study. Section II details the application of GPR in predicting ZWD. Section III encompasses the experimental aspect, including comparative analysis of interpolation methods, and other pertinent evaluations. Section IV presents a summary of our research findings and conclusions.

II. Methodology

This section presents the methodology employed in this study to estimate ZWD using GPR and compare its performance with the ordinary kriging method. We discuss the calculation of ZWD values at reference stations using PPP, the application of ordinary kriging for ZWD estimation, and the proposed GPR algorithm. This section also highlights the advantages of using PPP-derived ZWD values as a reference and the importance of selecting appropriate kernel functions and hyperparameters in the GPR model.

A. ZWD Calculation and Data Processing

As we mentioned before, the ZWD values of reference stations are the key input in this article, which are calculated by the dual-frequency ionosphere-free combination model. PPP is a well-established and widely used method that can estimate ZWD with high precision. One of the main advantages of PPP is its ability to process each station independently, without relying on a reference station network. This simplifies the computation process and makes the implementation more straightforward.

TABLE I
SUMMARY OF METHODS AND MODELS FOR ADDRESSING ZWD ERROR IN GNSS

Methods/Models	Key Assumptions	Limitations
Empirical models (Saastamoinen, Hopfield, Unifrom Atmosphere Tropospheric Error Model) [11], [12], [13], [10], [30]	Rely on atmospheric parameters (temperature, pressure, humidity)	Parameters often derived from ZWD data
Traditional interpolation methods (DIM, LIM, LCM, LSM) [19], [20], [21], [5], [22], [23], [31], [32]	linear assumption	Limited accuracy in areas with complex tropospheric variations
Ordinary Kriging [2], [24], [25], [33], [34]	Spatial stationarity assumption	Assumption may be violated under specific weather conditions

TABLE II
SUMMARY OF THE STRATEGY OF DATA PROCESSING

Parameter	Strategy and Value
Position model	Static
Data Sampling interval	30 s
Constellation	GPS
Frequency	L1 and L2
Ionosphere	Ionospheric free
Satellite's orbit and clock	Precise ephemeris files (.sp3) and precise clock files (.clk) from Crustal Dynamics Data Information System
Zenith hydrostatic delay	Saastamoinen model
Zenith wet delay	Estimated
Ambiguity	Float

Furthermore, by using PPP, we can obtain ZWD estimates that serve as independent reference values, which is beneficial for comparing and validating the results from other methods. Although the network-based model in PPP-RTK can also estimate ZWD values at reference stations and improve the estimation accuracy by utilizing interstation constraints, the resulting estimates may be influenced by the network structure and constraint settings. Different network designs might lead to variations in the estimated values.

To ensure the independence and consistency of the reference station ZWD estimates, we have chosen to use the single-station PPP method in this study. The PPP-derived ZWD values can be considered as "true values" that are not affected by network constraints. This approach is more suitable for evaluating the performance of the Gaussian process interpolation, as the interpolation results will not be influenced by network adjustment effects.

It is worth noting that the network-based model in PPP-RTK has its own merits, and future research could consider comparing and analyzing the ZWD estimates from both PPP and PPP-RTK network-based models. However, for the purpose of this study, which focuses on assessing the performance of the Gaussian process interpolation method, using PPP-estimated ZWD values as a reference is more appropriate. The basic observation equations for code pseudorange P and carrier phase L observations are given by

$$P^s_{r,\mathrm{IF}} = \rho^s_r + t_r - t^s + m^s_r Z_r + b_{r,\mathrm{IF}} - b^s_{\mathrm{IF}} + e^s_{r,\mathrm{IF}} \quad (1)$$

$$L^s_{r,\mathrm{IF}} = \rho^s_r + t_r - t^s + m^s_r Z_r + \lambda_{\mathrm{IF}}\left(N^s_{r,\mathrm{IF}} + B_{r,\mathrm{IF}} - B^s_{\mathrm{IF}}\right) + \varepsilon^s_{r,\mathrm{IF}} \quad (2)$$

where ρ^s_r represents the geometric distance between the satellite s and receiver r; t_r and t^s denote the receiver and satellite clock offsets, respectively, $m^s_r Z_r$ accounts for the tropospheric delay; and $b_{r,\mathrm{IF}}$ and b^s_{IF} are the receiver and satellite hardware biases, respectively. The tropospheric dry delay can be effectively corrected using the widely adopted Saastamoinen model [35], leaving the tropospheric wet delay $m^s_{r,w} Z_{r,w}$ as the primary component to be considered. The satellite clock offset, t^s, can be corrected with precise products. The linearized observation equations for the ionosphere-free combination are expressed as

$$E\left(p^s_{r,\mathrm{IF}}\right) = \mu^s_r \cdot x + \hat{t}_{r,\mathrm{IF}} + m^s_{r,w} Z_{r,w} \quad (3)$$

$$E\left(l^s_{r,\mathrm{IF}}\right) = \mu^s_r \cdot x + \hat{t}_{r,\mathrm{IF}} + m^s_{r,w} Z_{r,w} + \lambda_{\mathrm{IF}} \hat{N}^s_{r,\mathrm{IF}} \quad (4)$$

where p^s_{IF} and $l^s_{r,\mathrm{IF}}$ denote the observed minus computed values for the ionosphere-free pseudorange and carrier phase observations, respectively; x represents the coordinate information to be estimated; and μ^s_r is the unit vector from the receiver to the satellite. Table II presents the key parameters and processing strategies employed in our GNSS data analysis.

B. Ordinary Kriging

This section describes the application of the ordinary kriging method for estimating ZWD at a user's location, utilizing observed ZWD values from reference stations [2], [24], [25]. The estimation, denoted as z_0, is computed as a weighted sum of the ZWD values from these stations

$$z_0 = \sum_i w_i z_i \quad (5)$$

where the weights (w_i) are determined based on the spatial correlation between each station and the user's location, which is quantified by the covariance function $C(h_{ij})$. This function represents the covariance between two points, i and j. The weights are obtained by solving the following system of linear equations:

$$\sum_i w_i C\left(h_{ji}\right) = C\left(h_{j0}\right) \quad (6)$$

$$\sum_i w_i = 1. \quad (7)$$

These equations ensure that the estimation accurately reflects the spatial correlation among observed ZWD values, considering the spatial separation (h_{ji}) between reference

stations and the user's location. The variogram function, $\gamma_{ji} = C(0) - C(h_{ji})$, indicates the variability of ZWD values with distance. AI-Shaery et al. [24] compared three semivariogram models, namely, the spherical, exponential, and Gaussian models, and concluded that their accuracies are comparable. Based on their findings, we opted to employ the exponential model in this study

$$C(h_{ji}) = b\left(1 - \exp\left(-\frac{h_{ij}}{a}\right)\right) \tag{8}$$

where h_{ij} is the distance between points i and j in space, and b and a denote the sill and range parameter of the variogram, respectively. This model assumes that spatial correlation decays exponentially with distance, and when the distance exceeds the range parameter a, the correlation approaches zero. This model implicitly assumes that the spatial process is isotropic and second-order stationary, which means: 1) spatial correlation depends only on the distance between points and is independent of direction (isotropy) and 2) the mean and variance of the spatial process are constant throughout the domain and the covariance is solely a function of the distance between points (second-order stationarity).

Ordinary kriging's assumption of stationarity and isotropy, which might not always be valid in meteorological studies, is noted. GPR is introduced as an alternative modeling approach to address potential nonstationarity in the ZWD estimation.

C. Gaussian Process Regression

In this study, we propose a GPR algorithm to estimate ZWD values using geographical location information provided by users, such as Cartesian coordinates. By employing kernel functions, we capture the complex patterns and nonlinearity in the data, enabling us to model the relationship between input features and ZWD values effectively.

Let $\mathbf{X}$ denote the input location information and $\mathbf{Z}$ represent the corresponding ZWD values. We assume an unknown function f that maps the location information $\mathbf{X}$ to the ZWD values $\mathbf{Z}$, which can be modeled as

$$\mathbf{z} = f(\mathbf{x}) + \boldsymbol{\epsilon} \tag{9}$$

where $\boldsymbol{\epsilon}$ represents the noise term, which is assumed to follow a normal distribution with zero mean and variance σ_ϵ^2, i.e., $\boldsymbol{\epsilon} \sim \mathcal{N}(0, \sigma_\epsilon^2)$.

We treat the outputs ($\mathbf{Z}$) as following a multivariate normal (MVN) distribution, with the mean vector $\boldsymbol{\mu}$ and covariance matrix $\boldsymbol{\Sigma}$ determined by the input data ($\mathbf{X}$):

$$\mathbf{Z} \sim \mathcal{N}(\boldsymbol{\mu}, \boldsymbol{\Sigma}). \tag{10}$$

When presented with new locations ($\boldsymbol{\chi}$) lacking observations but requiring ZWD predictions ($\mathbf{Z}(\boldsymbol{\chi})$), we construct a joint Gaussian process prior that encompasses both the observed values $\mathbf{Z}$ and the predictions $\mathbf{Z}(\boldsymbol{\chi})$, which are also denoted as $\mathbf{Z}^*$

$$\begin{bmatrix} \mathbf{Z} \\ \mathbf{Z}(\boldsymbol{\chi}). \end{bmatrix} \sim \mathcal{N}\left(\begin{bmatrix} \boldsymbol{\mu} \\ \boldsymbol{\mu}_{\boldsymbol{\chi}}. \end{bmatrix}, \begin{bmatrix} \boldsymbol{\Sigma} & \boldsymbol{\Sigma}(\mathbf{X}, \boldsymbol{\chi}) \\ \boldsymbol{\Sigma}(\mathbf{X}, \boldsymbol{\chi})^\top & \boldsymbol{\Sigma}(\boldsymbol{\chi}, \boldsymbol{\chi}). \end{bmatrix}\right). \tag{11}$$

Leveraging the proximity of $\mathbf{Z}(\boldsymbol{\chi})$ to $\mathbf{Z}$ values corresponding to similar $\mathbf{X}$ entries, we can obtain the predictive distribution $\mathbf{Z}(\boldsymbol{\chi})|\mathbf{Z}$ by standard MVN conditioning, with the mean and covariance given by

$$\boldsymbol{\mu}_{\mathbf{Z}}(\boldsymbol{\chi}) = \boldsymbol{\Sigma}(\boldsymbol{\chi}, \mathbf{X})\boldsymbol{\Sigma}^{-1}\mathbf{Z} \tag{12}$$

$$\boldsymbol{\Sigma}_{\mathbf{Z}}(\boldsymbol{\chi}) = \boldsymbol{\Sigma}(\boldsymbol{\chi}, \boldsymbol{\chi}) - \boldsymbol{\Sigma}(\boldsymbol{\chi}, \mathbf{X})\boldsymbol{\Sigma}^{-1}\boldsymbol{\Sigma}(\mathbf{X}, \boldsymbol{\chi}). \tag{13}$$

The central aspect of our discussion revolves around the selection of the covariance function $\boldsymbol{\Sigma}(\cdot, \cdot)$ in (10). When selecting the covariance function $\boldsymbol{\Sigma}(\cdot, \cdot)$, we must ensure that it remains finite and positive definite to serve as a valid MVN covariance structure. To achieve this, we choose exponential kernels where its radial decay depends on the distance between data points. The mathematics equation for the exponential kernel is as follows:

$$k_\theta^p(\mathbf{x}_i, \mathbf{x}_j) = \exp\left\{-\frac{||\mathbf{x}_i - \mathbf{x}_j||^p}{\theta}\right\}. \tag{14}$$

In this kernel function, $||\ \cdot\ ||$ denotes the $L2$ norm of the vector. This scaling parameter, θ, often referred to as the characteristic length scale, is crucial for controlling the smoothness of the resulting stochastic process. The exponential kernel function measures the similarity between spatial points. When two points are close, the kernel function value is close to 1, indicating strong correlation; when two points are farther away, the kernel function value tends to 0, indicating weak correlation. By adjusting the scale parameter l, the decay rate of correlation can be controlled. Unlike the exponential variogram function, the exponential kernel function does not directly assume the stationarity and isotropy of the spatial process. It pays more attention to the local similarity between the spatial points and portrays the spatial correlation structure by the magnitude of the kernel function.

To determine the optimal parameters θ for our covariance function, we define the objective function $f(\theta)$ as the negative log-likelihood function, which measures how well our model with parameters θ fits the observed data

$$f(\theta) = -\log \mathcal{L}(\mathbf{Z}; \theta) \tag{15}$$

where $\mathcal{L}(\mathbf{Z}; \theta)$ is the likelihood of observing the data $\mathbf{Z}$ given the parameters θ. The negative log-likelihood function can be expressed as

$$f(\theta) = \frac{1}{2}\mathbf{Z}^T\mathbf{K}(\theta)^{-1}\mathbf{Z} + \frac{1}{2}\log|\mathbf{K}(\theta)| + \frac{n}{2}\log 2\pi \tag{16}$$

where $\mathbf{K}(\theta)$ is the covariance matrix parameterized by θ. The elements of $\mathbf{K}(\theta)$ are given by $\mathbf{K}(\theta)_{ij} = k_\theta^p(\mathbf{x}_i, \mathbf{x}_j)$, and n is the number of observations.

Another hyperparameter in (14), denoted as p, must be positive and is typically chosen based on domain knowledge or experimental design rather than being inferred from data. The choice of p significantly affects the smoothness of the stochastic process; for example, setting $p = 2$ results in the Gaussian or squared exponential kernel, which produces a Gaussian process characterized by infinitely smooth and mean-square differentiable realizations. Conversely, when $p \neq 2$, the process becomes nondifferentiable. In this article, we estimate the ZWD, which often exhibits sharp local variations. We chose the exponential kernel for our GPR model due to its ability to capture these variations effectively. This kernel decays more gradually than smoother alternatives such as Gaussian,

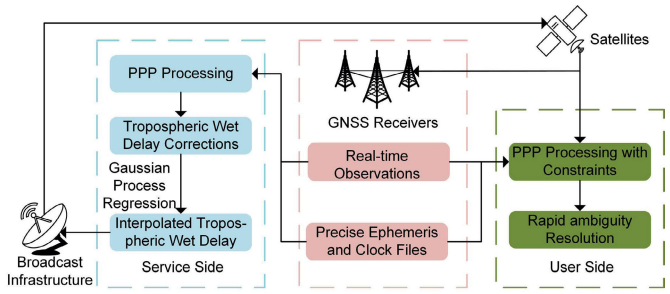

Fig. 1. Schematic for tropospheric wet delay estimation and user positioning.

making it well suited for modeling nonsmooth, localized patterns without oversmoothing the data. In addition, it strikes a good balance between model flexibility and computational simplicity, offering both accuracy and efficiency when compared to more complex kernels such as Matérn. The complete process of estimating ZWD values using GPR is detailed in Algorithm 1.

Algorithm 1 Estimating ZWD Values Using GPR

Require: Initial parameter vector $\theta_0 \in \mathbb{R}^n$, lower bounds $lob \in \mathbb{R}^n$, upper bounds $upb \in \mathbb{R}^n$, input data: $\mathbf{Z} = \{Z_1, Z_2, \ldots, Z_m\}$ and $\mathbf{P} = \{\mathbf{P}_1, \mathbf{P}_2, \ldots, \mathbf{P}_m\}$

Ensure: Optimized parameter vector $\theta^* \in \mathbb{R}^n$.

1: Calculate inter-parameter correlation matrix $\mathbf{K} \in \mathbb{R}^{m \times m}$ using Eq.14;
2: Define the objective function $f(\theta)$ by Eq.15;
3: **while** θ is not optimal **do**
4: Initialize the optimization process: θ_0 and parameter boundaries $[lob, upb]$;
5: Evaluate the gradient $\nabla f(\theta_t)$ and define the search direction $\mathbf{d} = -\nabla f(\theta_t)$ (gradient descent direction);
6: Adjust parameters: $\theta_{t+1} = \theta_t + \alpha \mathbf{d}$, where α determined by backtracking line search is the step size;
7: Evaluate the objective function $f(\theta_{t+1})$ and update θ;
8: **end while**
9: Calculate ZWD values $\mathbf{Z}^*$ by Eq.12 and Eq.13.
10: **return** Estimated ZWD values $\mathbf{Z}^*$.

The schematic, which is shown in Fig. 1, illustrates the architecture and workflow of a rapid PPP system for estimating tropospheric wet delays and achieving high-accuracy user positioning. The system consists of three main components: the broadcast infrastructure, the GNSS receivers, and the user-side processing. The GNSS receivers collect real-time observations and precise orbit and clock data, which are essential inputs for both the service-side PPP processing and the user-side PPP processing with constraints.

On the service side, the broadcast infrastructure includes a GNSS satellite constellation and the PPP processing module. The PPP processing module utilizes the collected GNSS observations and precise orbit and clock data to estimate tropospheric wet delay corrections using GPR. The interpolated tropospheric wet delays are then transmitted to the user side via the broadcast infrastructure. On the user side, the PPP processing module receives the interpolated tropospheric wet delays as constraints. By integrating these constraints into the user-side PPP processing, the system achieves rapid ambiguity resolution and improved positioning accuracy.

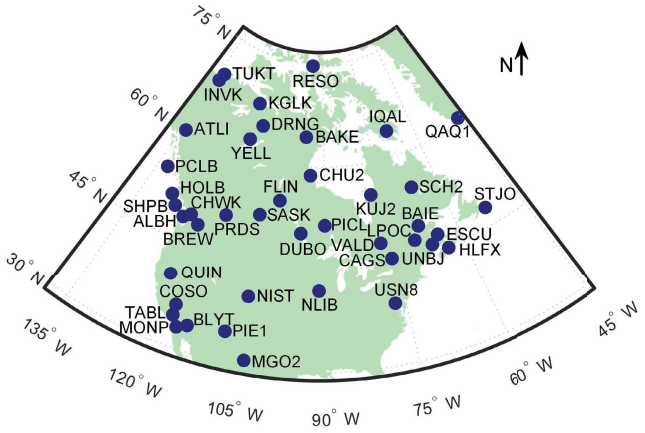

Fig. 2. Spatial distribution of the 53 reference stations across North America.

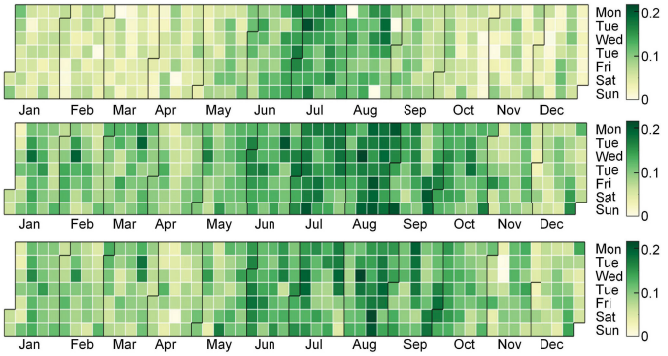

Fig. 3. Annual variation of ZWD calculated by PPP for 2022 at (top) INVK, (middle) ALBH, and (bottom) BREW reference stations.

III. Numerical Results

In this section, we present our experimental analysis and the resulting findings. Our study focused on the analysis of ZWD values from reference stations across North America, as well as a smaller network in Hong Kong, for the year 2022. This analysis was conducted using PPP algorithms and observational data. It is noteworthy that in this study, we set the initial θ to 1, with a lower bound of 0.01 and an upper bound equal to $\max(h_{ij})$.

A. North American Network

To compare the fitting accuracy and computational efficiency of GPR and ordinary kriging, as well as to investigate the impact of the stationarity assumption on their performance, we employed data from 39 reference stations across North America. The spatial distribution of these reference stations is shown in Fig. 2. This large-scale network covers a wide range of latitudes, from 30°N to 75°N, and longitudes, from 135°W to 45°W, encompassing diverse climatic and topographic conditions.

The network in North America is larger and more complex, with varying ZWD values across the reference stations. Fig. 3 illustrates the heatmaps of ZWD values for three selected

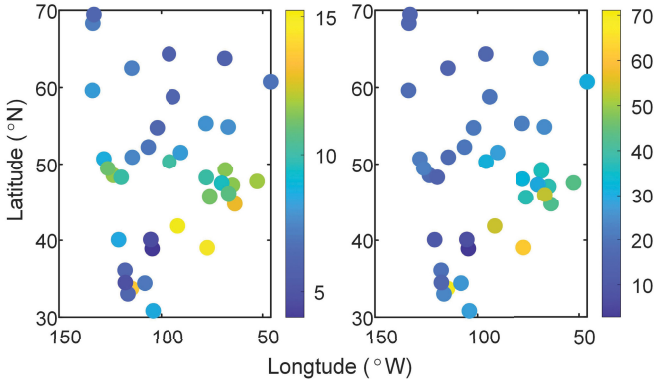

Fig. 4. Mean and variance of ZWD for 39 GNSS reference stations in North America (2022).

reference stations (BREW, ALBH, and INVK) over the course of a year in 2022. It is worth noting that BREW and ALBH are geographically close to each other, while INVK is located farther away from the other two stations.

The heatmaps reveal distinct seasonal patterns in the ZWD values for all three reference stations, with the highest values occurring during the summer months. However, a closer examination reveals that the ZWD heatmaps of BREW and ALBH exhibit greater similarity to each other compared to INVK, which displays more pronounced differences. This observation suggests that the spatial proximity of reference stations may influence the similarity of their ZWD patterns.

1) Second-Order Stationary Analysis: Ordinary kriging assumes second-order stationarity of the data, making it essential to verify whether our dataset satisfies this assumption. The purpose of this section is to assess the spatial variability and correlation of ZWD across the North American GNSS network to validate the feasibility of applying ordinary kriging. Fig. 4 presents the mean and variance of the annual ZWD time series at each of the 39 stations. The mean ZWD values span a range of approximately 10 cm between the lowest and highest stations, while variances fluctuate considerably from 10 to 70 cm^2.

To further investigate stationarity, we examine the ZWD correlations between station pairs. Taking station KUJ2 as an example (highlighted in red), Fig. 5 (top) plots the CC with the nine stations exhibiting the strongest correlations to KUJ2, such as BAIE (0.60), CAGS (0.73), and VALD (0.86), all falling between 0.5 and 0.9. In contrast, Fig. 5 (bottom) shows the nine stations with the weakest correlations to KUJ2, such as HOLB (0.03), INVK (−0.46), and PRDS (−0.20). Many of these correlations are very low or negative, departing substantially from the assumption of second-order stationarity.

The CC is a statistical measure of the strength and direction of the linear relationship between two variables, with values ranging from −1 to 1. A value of 1 indicates a perfect positive correlation, meaning that as one variable increases, the other variable increases proportionally. A value of 0 suggests no linear relationship between the two variables.

The analysis of the North American reference station network reveals that it is complex and variable. Inputting ZWD information from all stations into the interpolation schemes

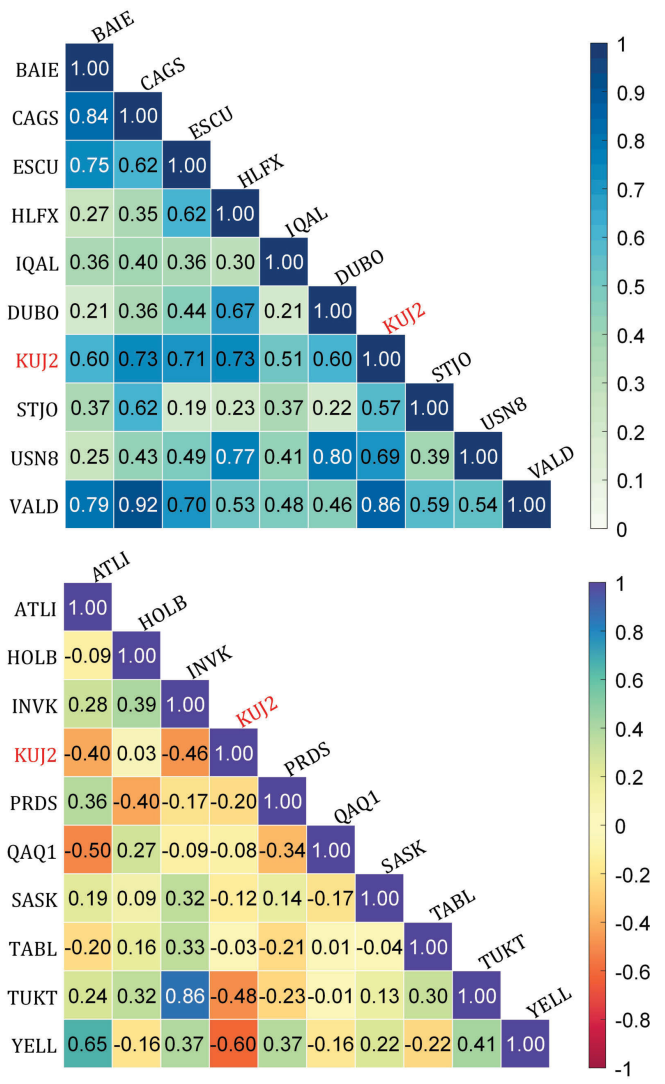

Fig. 5. CC matrix of ZWD at North American reference stations. (Top) Nine stations most and (bottom) least correlated with KUJ2 in 2022.

may be ill-advised, as it could lead to inaccurate results due to the violation of the second-order stationarity assumption.

In Sections III-A2 and III-A3, we will investigate how the similarity characteristics of the North American network affect the performance of GPR and ordinary kriging in modeling and estimating ZWD values, taking into account the proposed correlation-based station filtering approach.

2) Comparative Analysis of GPR and Ordinary Kriging Under Different Correlation Thresholds: Based on Fig. 5, we can conclude that in the North American region, the CC between reference stations varies significantly.

Theoretically, setting a higher CC threshold should lead to better interpolation results for both methods. However, when we set the threshold to 0.8, only six reference stations (ALBH, BAKE, BREW, CHU2, TUKJ, and YELL) have more than two reference stations that satisfy this threshold. This implies that if the threshold is set to 0.8, most areas in North America will not have sufficient input information for GPR and ordinary kriging interpolation.

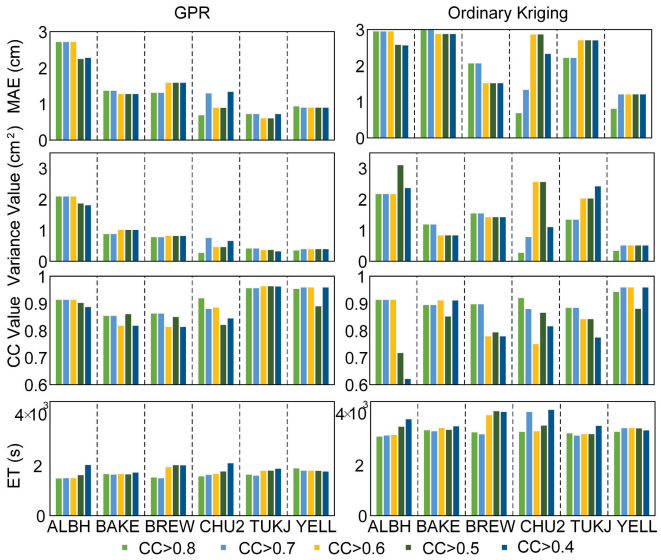

Fig. 6. Comparison of GPR and ordinary kriging for ZWD estimation at six stations by MAE, variance, CC, and ET under different CC thresholds.

To determine how the CC threshold affects the performance of GPR and ordinary kriging and to select an appropriate threshold value, we conducted interpolation experiments on the aforementioned six reference stations, setting the threshold to CC $>$ 0.8, 0.7, 0.6, 0.5, and 0.4. We compared the interpolation results based on four metrics: mean absolute error (MAE), variance, CC, and execution time (ET). The MAE represents the average of the absolute bias values, where the bias value is defined as the difference between the estimated value and the true value. As shown in Fig. 6, GPR consistently outperforms ordinary kriging across all metrics, and the performance of ordinary kriging is more sensitive to changes in the CC threshold. In contrast, the interpolation results of GPR are less affected by different CC thresholds.

Theoretically, as the threshold decreases from 0.8 to 0.4, the MAE should gradually increase. This trend is observed for CHU2, TUKJ, and YELL. However, ALBH, BAKE, and BREW exhibit a slight decrease in MAE on the right side of the figure, which can be attributed to the inclusion of reference stations with mean values closer to the target station when the threshold is lowered. As the threshold decreases from 0.8 to 0.4, the CC coefficients of all reference stations decrease, while the ET increases, which is consistent with theory.

Our experiments demonstrate that GPR outperforms ordinary kriging across all metrics and is less sensitive to changes in the CC threshold. As the threshold decreases, the MAE generally increases, although some reference stations may experience a slight decrease due to the inclusion of stations with similar mean values. The runtime also increases as the threshold is lowered, as more reference stations are included in the interpolation process.

3) Interpolation Performance of Two Methods Across Different Categories of Reference Stations: While we have compared the fitting performance of ordinary kriging and GPR across multiple dimensions under different CC values, the analysis was limited to only six reference stations that met the criterion of CC $>$ 0.8. This implies that our validation has been confined to a few localized areas in North America. Therefore, in this section, we extend our investigation to validate the fitting performance of both methods across a broader range of North American regions.

To assess the interpolation performance of other reference stations in North America and investigate the impact of input data quantity on interpolation results under the same threshold CC $>$ 0.5, we designed the following experiment. Based on the number of other reference stations satisfying the threshold, the reference stations were divided into three categories.

1) *Well-Connected Stations:* The number of other reference stations satisfying the threshold is greater than 5.
2) *Moderately Connected Stations:* The number of other reference stations satisfying the threshold is 4 or 5.
3) *Poorly Connected Stations:* The number of other reference stations satisfying the threshold is less than or equal to 3.

For each category, we selected four reference stations and compared the interpolation performance of GPR and ordinary kriging by evaluating the CC and root-mean-square (rms) error. The rms error, which quantifies the average magnitude of estimation errors, is calculated as

$$\text{rms} = \sqrt{\frac{\sum_{i=1}^{n}\left(Z_{\text{pred},i} - Z_{\text{true},i}\right)^2}{n}}. \tag{17}$$

As shown in Fig. 7, under a threshold of 0.5, most reference stations exhibited higher CC and lower rms values for GPR compared to ordinary kriging. For instance, in Fig. 7, when MGO2 and ALBH were used as user stations, the CC and rms values for GPR interpolation were 0.9545 and 0.7327 cm for MGO2, and 0.9030 and 1.5364 cm for ALBH, respectively. In contrast, the CC and rms values for ordinary kriging interpolation were 0.7218 and 3.6495 cm for MGO2, and 0.6946 and 3.5307 cm for ALBH, respectively.

However, some reference stations, such as VALD in Fig. 8, demonstrated lower CC but smaller rms values for GPR compared to ordinary kriging. In this case, the CC and rms values for GPR interpolation were 0.8148 and 1.6043 cm, while those for ordinary kriging were 0.8582 and 2.3967 cm, respectively. Conversely, some reference stations, such as STJO in Fig. 9, exhibited higher CC but larger rms values for GPR compared to ordinary kriging. For STJO, the CC and rms values for GPR interpolation were 0.6360 and 5.8863 cm, while those for ordinary kriging were 0.6281 and 5.7770 cm, respectively.

A comprehensive analysis of these results suggests that GPR is generally superior to ordinary kriging for interpolation in North America. Furthermore, we observed that poorly connected stations consistently performed worse than well-connected and moderately connected stations in terms of both CC and rms values. This indicates that regardless of the interpolation method employed, input data from at least moderately connected stations are necessary to obtain accurate interpolation results.

Within the same category of reference stations, we observed varying degrees of interpolation performance. For some stations, GPR significantly outperformed ordinary kriging, while for others, the performance of GPR was comparable to that

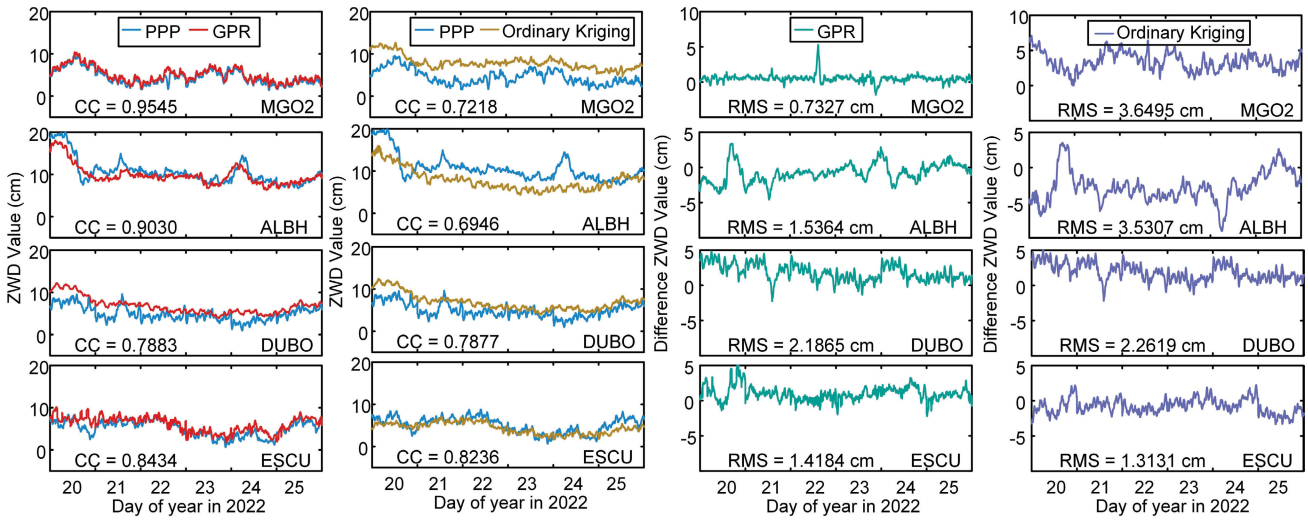

Fig. 7. Comparison of the six-day ZWD values from PPP and estimations at four well-connected stations and time series of their differences.

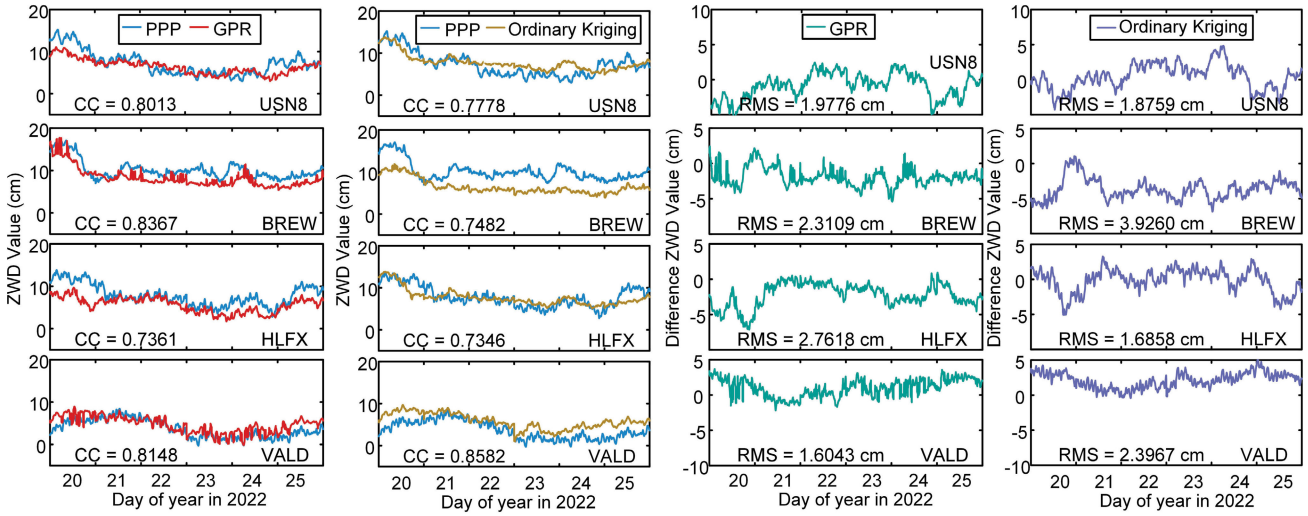

Fig. 8. Comparison of the six-day ZWD values from PPP and estimations at four moderately connected stations and time series of their differences.

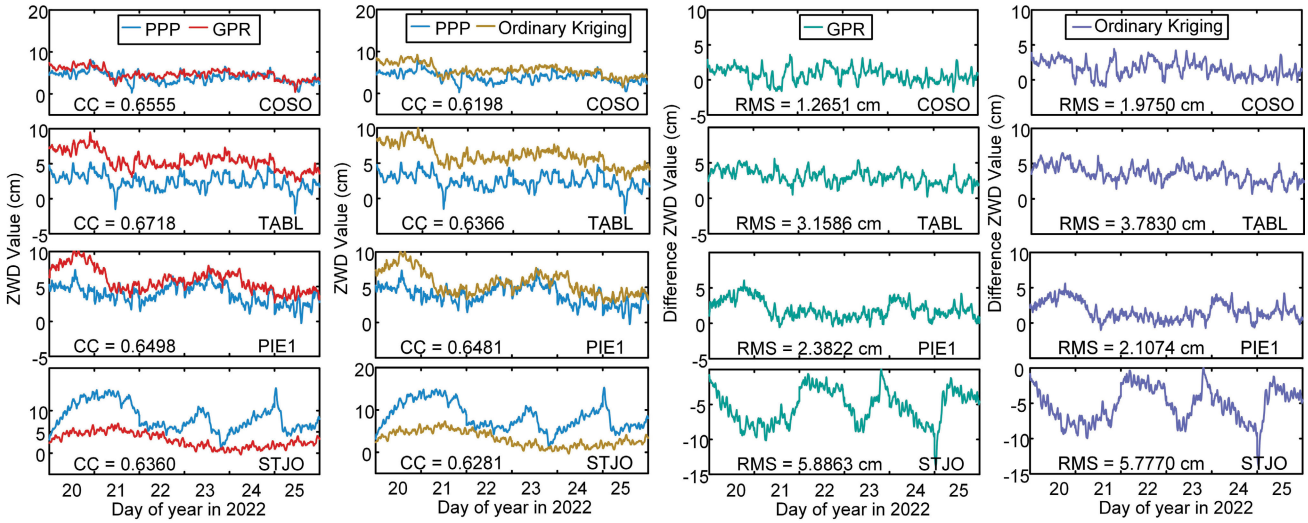

Fig. 9. Comparison of the six-day ZWD values from PPP and estimations at four poorly connected stations and time series of their differences.

of ordinary kriging. Upon analyzing the data characteristics of these reference stations, we found that those exhibiting substantial performance differences had input data containing CC greater than 0.8. These highly correlated data points provide GPR with more representative samples, enabling it to better generalize overall patterns.

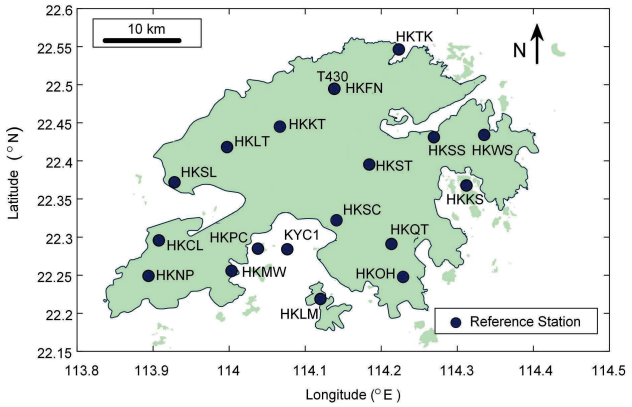

Fig. 10. Spatial distribution of the 19 reference stations across Hong Kong.

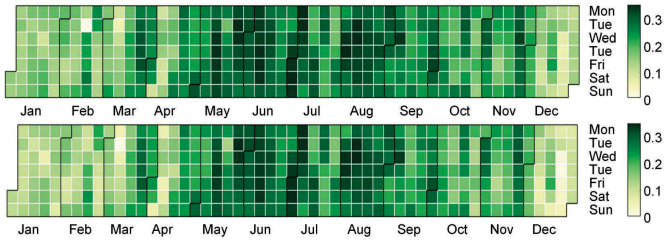

Fig. 11. Annual variation of ZWD calculated by PPP for 2022 at (top) HKNP and (bottom) HKSS reference stations.

In this section, we evaluated the interpolation performance of GPR and ordinary kriging for reference stations in North America, categorizing the stations based on the number of connected stations satisfying a given threshold. The results demonstrated that GPR generally outperformed ordinary kriging. The analysis also revealed that interpolation accuracy improves with an increasing number of connected stations, emphasizing the importance of having input data from at least moderately connected stations for reliable interpolation results.

B. Hong Kong Network

To further investigate ZWD patterns and compare the performance of GPR and ordinary kriging, we extended our analysis to a denser network of reference stations. This expanded dataset allows for a more comprehensive assessment of the two methods' capabilities in capturing spatial variations and provides insights into their suitability for modeling ZWD in regions with varying station densities.

The spatial distribution of these Hong Kong reference stations is illustrated in Fig. 10. This localized study allows us to examine ZWD characteristics within a specific region. The heated figures of ZWD values, as depicted in Fig. 11, calculated using PPP at the HKNP and HKSS reference stations in Hong Kong throughout 2022 reveal a generally consistent distribution pattern. This similarity can be attributed to the geographical proximity of the reference stations in Hong Kong, which supports the rationale for employing ordinary kriging in our study, as it requires the assumption of stationarity, as mentioned in Section II. In addition, this figure reveals clear seasonal fluctuations in ZWD values. These fluctuations are primarily attributed to changes in atmospheric water vapor

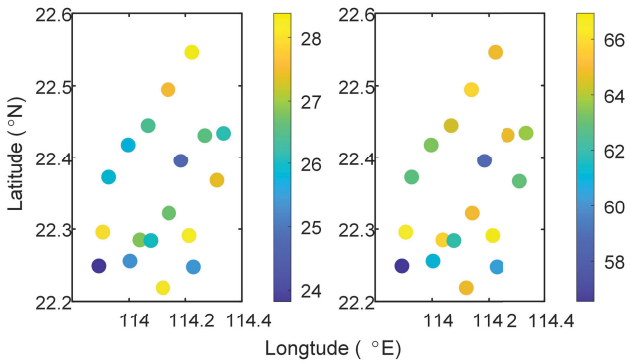

Fig. 12. (Left) Mean and (right) variance of ZWD for 19 GNSS reference stations in Hong Kong over the year 2022.

levels, which are influenced by temperature variations and weather patterns that vary with the seasons.

It is worth noting that the ZWD values at other reference stations in Hong Kong during this year exhibit similar patterns to those shown in Fig. 11. For the sake of conciseness, not all of them are presented here. The occasional blank spaces in the heatmaps do not indicate zero ZWD values on those particular days; rather, they are a result of missing data in the observation files. Nevertheless, such occurrences are infrequent and do not happen simultaneously across multiple reference stations. Subsequent fitting and experimental results demonstrate that this phenomenon has a negligible impact on the estimation of ZWD values.

1) Second-Order Stationarity Analysis: Before applying GPR and ordinary kriging for interpolation in the Hong Kong network, it is crucial to assess the second-order stationarity of ZWD across the reference stations.

Fig. 12 presents the mean and variance of ZWD for each of the 19 reference stations using data from the entire year of 2022. The mean ZWD values in the Hong Kong region range from 24 to 28 cm, while the variances fall between 55 and 66 cm. Although the mean and variance values differ slightly among stations, they remain relatively close, indicating a degree of spatial consistency in ZWD across the network. To further investigate the spatial correlation, we computed the CC between the ZWD time series of all station pairs, as shown in Fig. 13. In our analysis, the CC among all reference stations is consistently high. The lowest the CC value is 0.97, observed between station pairs such as HKCL and HKKS, as well as HKTK and KYC1. The highest CC values reach 0.99, found between station pairs such as HKOH and HKPC, and HKST and HKWS. These high CC demonstrate that the temporal trends of ZWD are highly similar among the different stations, supporting the assumption of spatial stationarity required for ordinary kriging.

The observed spatial consistency and strong correlation of ZWD values among the Hong Kong GNSS stations provide evidence supporting the second-order stationarity assumption. This finding validates the applicability of ordinary kriging for spatially interpolating ZWD values across the network, which will be further explored in Sections III-B2–III-B4.

2) General Performance Comparision: In this section, we assess the accuracy and efficiency of ordinary kriging and

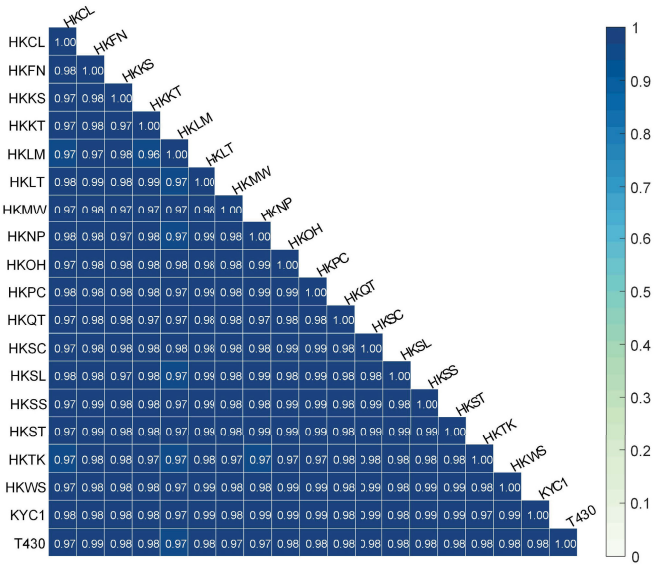

Fig. 13. CC matrix of ZWD time series between all pairs of the 19 GNSS reference stations in Hong Kong in 2022.

TABLE III
COMPARISON OF GPR AND ORDINARY KRIGING: MAE, ET, AND THEIR RATIO

Reference Stations	GPR		Ordinary Kriging		MAE Ratio	Time Ratio
	MAE (m)	ET (s)	MAE (m)	ET (s)		
HKSC	0.0061	1710.46	0.0060	5874.23	0.99	3.43
HKLM	0.0217	1535.21	0.0210	5394.19	0.97	3.51
HKPC	0.0062	1545.44	0.0060	5544.78	0.97	3.59
HKOH	0.0135	1545.00	0.0137	5404.00	1.00	3.59
HKSS	0.0094	1540.21	0.0096	5511.74	1.03	3.58
HKCL	0.0312	1564.48	0.0289	5321.30	0.92	3.40
HKFN*	**0.0081**	**1592.21**	**0.0140**	**3861.12**	**1.72**	**2.43**
T430*	**0.0081**	**1572.74**	**0.0128**	**3874.41**	**1.58**	**2.46**
HKKS	0.0258	1506.66	0.0254	5278.72	0.99	3.50
HKKT	0.0071	1508.22	0.0072	5265.62	1.02	3.49
HKLT	0.0101	1542.40	0.0107	5458.85	1.06	3.54
HKMW	0.0340	1550.07	0.0347	5448.23	1.02	3.51
HKNP	0.0371	1600.88	0.0376	5229.95	1.01	3.27
HKQT	0.0191	1554.77	0.0184	5378.97	0.96	3.46
HKSL	0.0150	1611.65	0.0156	5613.70	1.04	3.48
HKST	0.0296	1546.27	0.0298	5483.30	1.01	3.55
HKTK	0.0258	1558.62	0.0255	5302.01	0.99	3.40
HKWS	0.0132	1533.79	0.0136	5386.34	1.03	3.51
KYC1	0.0245	1522.07	0.0249	5355.33	1.01	3.52

GPR in interpolating ZWD values across multiple reference stations in Hong Kong. The performance of these two methods will be evaluated and compared to determine their suitability for estimating ZWD values in the given geographical context.

The core of this evaluation, presented in Table III, centers on comparing the estimation accuracy and computational efficiency of both methods. To further elucidate our findings, we introduce the "Ratio" metric, calculated as the value of GPR divided by that of ordinary kriging for each corresponding measure. As a result, a ratio value below 1 indicates that ordinary kriging exhibits lower accuracy or higher ET compared to GPR.

Our analysis indicates that the MAE ratio value is approximately 1, demonstrating that the accuracy of ordinary kriging and GPR is comparably accurate. However, a significant distinction emerges in terms of computational efficiency. The computational time ratio, estimated to be around 3.5, reveals that ordinary kriging demands nearly triple the time required by GPR for computation. This substantial difference in computational efficiency stems from the fact that ordinary kriging necessitates the estimation of two parameters, namely, the sill and range, for its variogram model. This process is notably computationally intensive, often requiring iterative optimization to determine the optimal fit. Conversely, GPR involves the estimation of a single parameter, denoted as θ, for its kernel function. This parameter in GPR can be optimized more directly and efficiently. GPR achieves similar accuracy levels as ordinary kriging, with the added benefit of greater ET efficiency. Practically speaking, the adoption of GPR can significantly reduce estimation time, thereby saving energy and potentially decreasing financial costs associated with extensive computational processes.

An intriguing deviation is observed for reference stations HKFN and T430, as highlighted in bold in Table III. When these two stations were utilized as user points, the bias in ZWD estimations from ordinary kriging was significantly higher than that from GPR. Furthermore, the time ratios for these two stations are lower than those for other stations. This indicates that when HKFN and T430 are used as "user," the difference in accuracy between ordinary kriging and GPR is larger than in normal situations, while simultaneously, the execution speed of ordinary kriging for these stations is quicker compared to other stations.

To find out the reasons for this situation, we need to analyze the variogram model. To compare different epoch times, we find two kinds of estimated variogram model results, which are shown in Fig. 14. When a normal variogram model is fit with a higher number of iterations, as shown in Fig. 14 (top), its sill and range parameters are reasonable, and the model (represented by a solid line) closely aligns with the empirical data points (indicated by dotted line). This precise estimation of spatial correlation allows for more accurate weighting of reference stations, leading to a nuanced interpolation that more accurately reflects the underlying distribution of ZWD values.

On the other hand, when the dataset has highly dispersed points, as shown in Fig. 14 (bottom), the rapid convergence of the model to a mean level indicates an oversimplification of spatial structures. The range is pretty low close to 0, while the sill reaches the mean line quickly. In such cases, the model tends to assign equal weights to all reference stations, disregarding spatial correlation and leading to a homogenized interpolation shown in Fig. 15. This results in a failure to capture the spatial variability of ZWD values, which is crucial for accurate regional predictions.

This comparison highlights the importance of a well-sampled dataset for effective use of ordinary kriging. A sparse dataset can lead to a flat variogram, incapable of capturing complex spatial variations, thereby limiting the effectiveness of the Kriging model. The necessity for an adequate number of evenly distributed observations across the study area is thus emphasized.

When a variogram model for ordinary kriging is fit with a dataset exhibiting high dispersion, the resulting plot shows this dispersion prominently. This leads to a rapid convergence

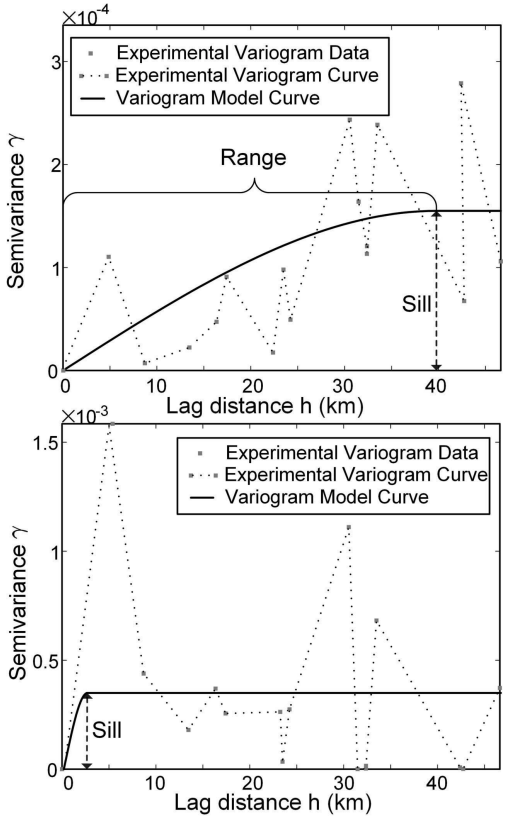

Fig. 14. Comparison of experimental variogram data and fit variogram model curves, showing (top) well-fit model and (bottom) suboptimal fit.

of the variogram model to a mean line, suggesting a lack of detailed spatial structure in the model. Consequently, the estimated ZWD values across the region end up reflecting an average of the reference stations rather than the actual spatial variations, as shown in Fig. 15 (bottom) for September 1, 2022 at 1:20 A.M. This is evident in the interpolation results, which resemble a horizontal cross-sectional plane, indicating a uniform ZWD value across the Hong Kong territory.

In contrast, employing GPR, a nonparametric Bayesian approach to regression, with the same dataset yielded significantly different results. GPR was able to discern subtle spatial variations in ZWD values, creating a topographically varied interpolation surface, as shown in Fig. 15 (top). This model successfully captured the inherent spatial heterogeneity of the atmospheric delays, reflecting different ZWD estimations at various locations. The reason for this phenomenon is because the exponential kernel function is different from the exponential variogram function, which is mentioned in Section II-C. The exponential kernel function does not directly assume stationarity and isotropy of spatial processes. It pays more attention to the local similarity between spatial points and portrays the spatial correlation structure through the magnitude of the kernel function value.

The clear difference in outcomes between ordinary kriging and GPR underscores the importance of selecting the right modeling technique for spatial data analysis. GPR was more capable of capturing and representing the complex spatial patterns in the ZWD data, proving its effectiveness in handling spatially dispersed datasets.

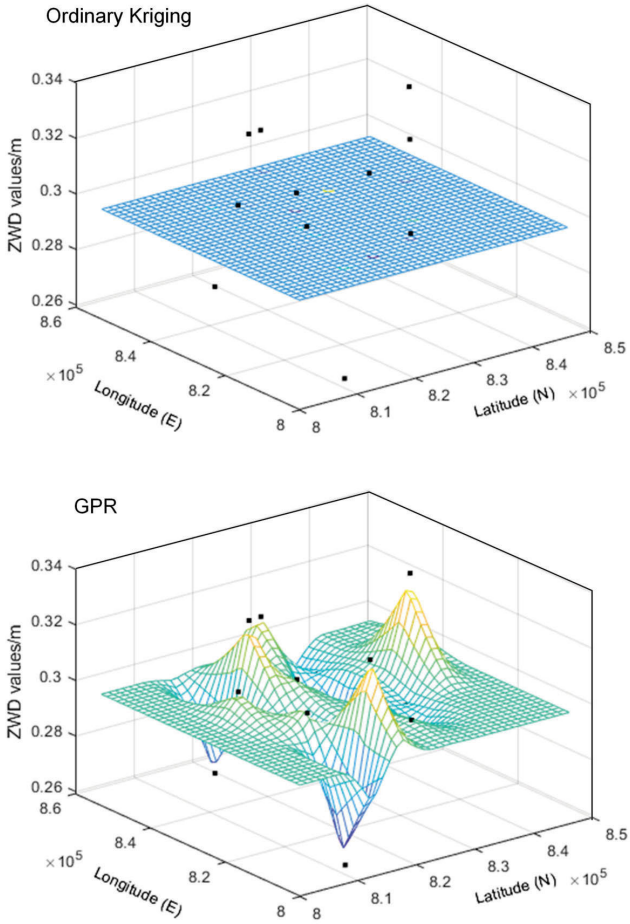

Fig. 15. Comparison of ZWD estimation surfaces over Hong Kong using (top) ordinary Kriging and (bottom) GPR methods.

3) Comparison of Consistency: This section compares the consistency of GPR and ordinary kriging methods. Although we have compared the mean bias in Section III-B1, the mean bias only reflects the overall estimation accuracy of the methods. A consistency comparison can reveal the stability of the methods across different time periods and stations.

Both GPR and ordinary kriging exhibit high consistency with the PPP results for ZWD estimation at each reference station. From the left of Fig. 16, it can be observed that the estimated values from GPR and ordinary kriging almost overlap with the PPP result curves, with CC above 0.94. This indicates that both methods can effectively fit the true ZWD time series.

Comparing Fig. 16, it is found that the consistency between GPR estimates and PPP results is marginally higher than that of ordinary kriging. At stations such as HKLM, HKSC, HKLT, HKTK, and HKWS, the CC of GPR is about 0.01 higher than that of ordinary kriging, indicating that GPR can capture the temporal variation characteristics of ZWD with a slight improvement.

From the rms errors on the right of Fig. 16, the rms values of GPR are marginally lower than those of ordinary kriging. Except for the HKSC station, the rms values of GPR are about 0.1–0.2 cm lower than those of ordinary kriging at other stations. This suggests that the GPR method has a minor

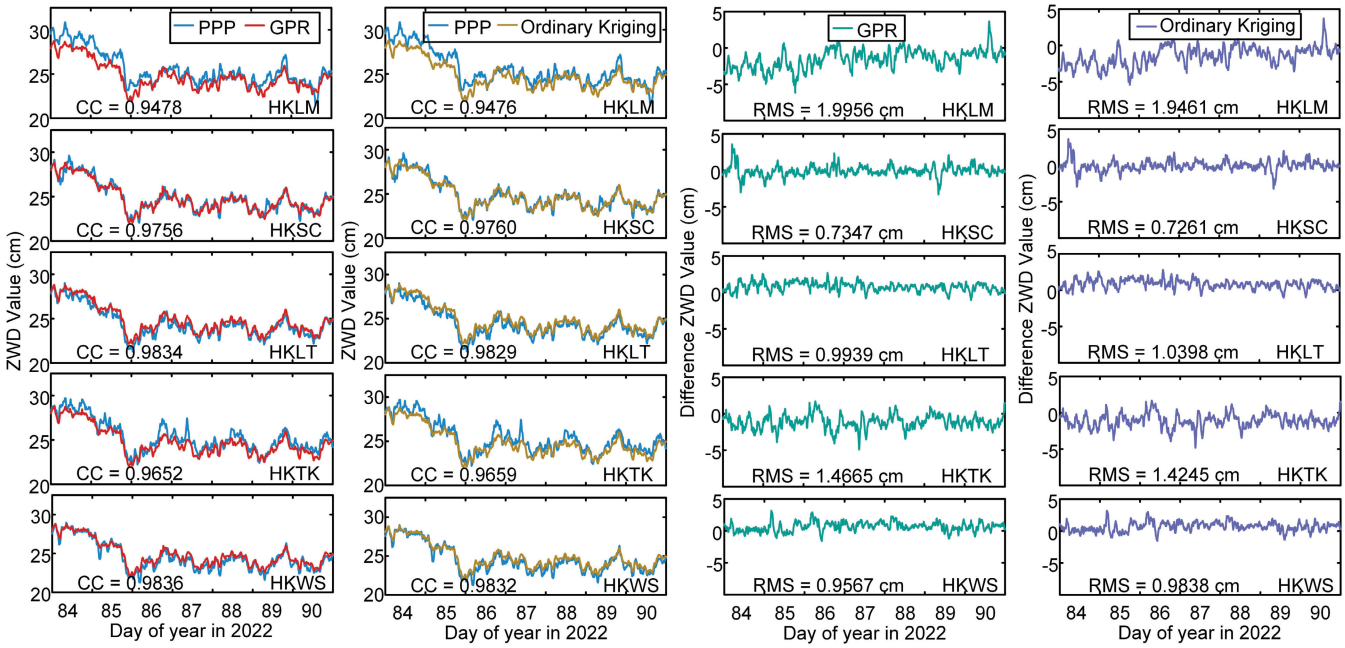

Fig. 16. Comparison of the seven-day ZWD values from PPP and GPR estimation at five Hong Kong reference stations and time series of their differences.

advantage in estimation accuracy. Slightly lower rms errors imply that GPR estimates have marginally lower dispersion and are somewhat closer to the ground truth values.

When the ZWD values from PPP exhibit sudden changes (i.e., the peaks in the figure), both GPR and ordinary kriging estimates show a certain smoothing effect and cannot fully capture these changes. This phenomenon exists to varying degrees at each station. For example, at the HKTK station, around the 87th day, the PPP results show a significant peak, but the estimates from GPR and ordinary kriging are relatively smooth and do not fit this change well. This is because both GPR and ordinary kriging assume that the variable to be estimated has a certain spatial correlation and smoothness. These assumptions are reflected in their mathematical models: GPR uses exponential kernels and ordinary kriging uses a semivariogram function with an exponential model, assuming gradual spatial variation.

While these assumptions are generally reasonable, they may not align with actual conditions at mutation points, where variable values differ significantly from surrounding values. Consequently, both methods may struggle to accurately capture these abrupt changes.

In summary, GPR demonstrates slightly better consistency and lower rms errors compared to ordinary kriging, though both methods show limitations in capturing sudden changes in ZWD values.

4) Localized Rainfall Pattern: The primary objective of this section is to evaluate and compare the performance of GPR and ordinary kriging in estimating ZWD values under nonstationary conditions.

To assess the performance of GPR and ordinary kriging in nonstationary scenarios, we selected two days, July 21, 2022, and December 21, 2022, both characterized by light and localized rainfall. Under such conditions, the spatial distribution of ZWD values is expected to be nonuniform, violating the assumption of stationarity. ZWD values were collected from multiple reference stations across the study area, as depicted in Fig. 17.

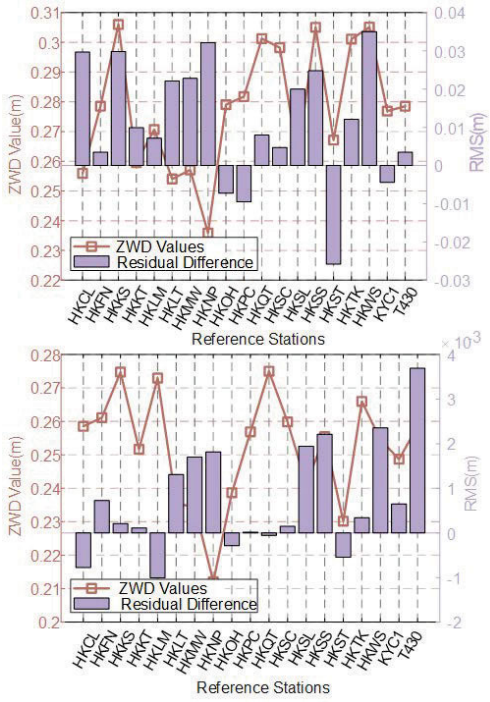

Fig. 17. Comparison of ZWD values and residual differences (absolute bias of ordinary kriging minus absolute bias of GPR) across reference stations on (top) July 21, 2022 and (bottom) December 21, 2022.

Both GPR and ordinary kriging were employed to interpolate ZWD values at each reference station. The interpolated ZWD values were then compared to the actual ZWD values, and the bias (difference between the interpolated and actual values) was calculated for each method. The absolute values of these biases were computed to facilitate a direct comparison between the two methods.

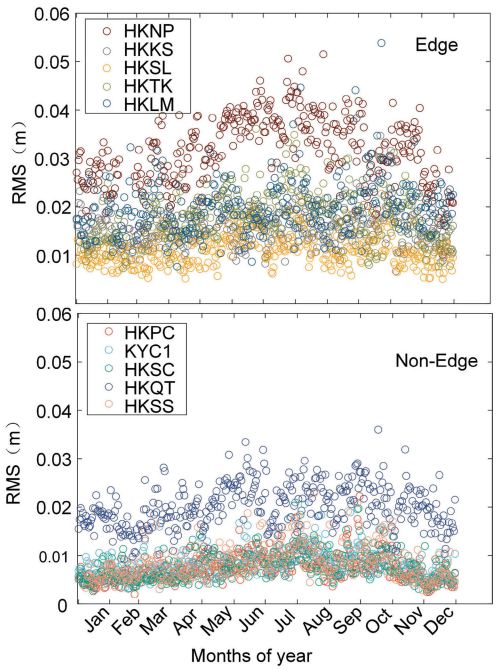

Fig. 18. RMS values of estimated ZWD at reference stations categorized by geographic location over a 12-month period. (Top) RMS values for edge reference stations. (Bottom) RMS values for nonedge reference stations.

Fig. 17 presents the ZWD values and the residual differences. The line plots demonstrate the significant variability in ZWD values across different reference stations, confirming the nonuniform spatial distribution of ZWD under localized rainfall conditions.

The bar plots in Fig. 17 illustrate the difference in absolute bias between ordinary kriging and GPR for each reference station. Positive values indicate that the absolute bias of ordinary kriging is higher than that of GPR, implying that GPR exhibits better accuracy in estimating ZWD values at those stations. Conversely, negative values suggest that ordinary kriging outperforms GPR in terms of accuracy.

The experimental results reveal that under nonstationary conditions induced by localized rainfall, GPR generally achieves higher accuracy in estimating ZWD values compared to ordinary kriging. This is evidenced by the predominantly positive residual differences between the absolute biases of the two methods, as shown in Fig. 17. The superior performance of GPR can be attributed to its ability to adapt to nonstationary spatial processes through the specification of a suitable covariance function, in contrast to ordinary kriging, which relies on the assumption of stationarity.

These findings underscore the importance of employing methods that can effectively handle nonstationary spatial processes when estimating ZWD values, particularly in the presence of localized precipitation events. GPR emerges as a promising approach for accurate ZWD estimation under such conditions.

5) Impact of Geographical Location: This section investigates the influence of geographical location of reference stations on the accuracy of GPR in estimating ZWD values. The rms error is employed as a metric to assess the accuracy of the estimated ZWD values. The rms error quantifies the average magnitude of the differences between the estimated and actual ZWD values, providing a measure of the overall estimation accuracy.

To assess the impact of geographical location, the reference stations were categorized into two groups: edge and nonedge stations. Edge stations are located along the periphery of the study area, while nonedge stations are situated within the interior of the region. Fig. 18 presents the rms values of the estimated ZWD at the edge and nonedge reference stations over a 12-month period.

The results indicate that the edge stations generally exhibit higher rms values compared to the nonedge stations, implying lower accuracy in ZWD estimation at the periphery of the study area. This observation can be attributed to the reduced spatial correlation between edge stations and their neighboring stations, as well as the potential extrapolation errors that may occur when estimating ZWD values near the boundaries of the region.

IV. Conclusion and Future Work

This research has demonstrated the advantages of GPR for ZWD estimation through comprehensive experiments in both Hong Kong and North America. Leveraging a year's worth of data from 39 stations across North America, we have shown that GPR delivers accurate ZWD predictions while reducing computation time compared to traditional methods such as ordinary kriging.

In the Hong Kong region, where the area is smaller and the reference stations are densely distributed, resulting in ZWD values that generally satisfy the stationarity assumption, the performance of GPR and ordinary kriging is comparable most of the time. However, we found that ordinary kriging does not always capture the spatial characteristics of ZWD distribution, whereas GPR consistently maintains its performance.

Thus, we conclude that GPR's robustness and adaptability to varying weather conditions and geographic contexts make it a versatile tool for ZWD estimation, especially in larger regions with more complex spatial variations.

Further research could investigate the integration of GPR with PPP-RTK, comparing and analyzing the ZWD estimates obtained from both methods to develop a more comprehensive and accurate ZWD estimation framework.

Acknowledgment

The authors would like to express their gratitude to the Crustal Dynamics Data Information System (CDDIS) and the Geodetic Survey Section, Survey and Mapping Office of the Lands Department (SATREF), for providing the GNSS data used in this study. The CDDIS data can be accessed at https://cddis.nasa.gov/, while the SATREF data can be available at https://www.geodetic.gov.hk/en/satref/satref.htm.

References

[1] J. L. Davis, T. A. Herring, I. I. Shapiro, A. E. E. Rogers, and G. Elgered, "Geodesy by radio interferometry: Effects of atmospheric modeling errors on estimates of baseline length," *Radio Sci.*, vol. 20, no. 6, pp. 1593–1607, Nov. 1985.

[2] H. Ma, Q. Zhao, S. Verhagen, D. Psychas, and H. Dun, "Kriging interpolation in modelling tropospheric wet delay," *Atmosphere*, vol. 11, no. 10, p. 1125, Oct. 2020.

[3] S. A.-M. Younes, "Modeling investigation of wet tropospheric delay error and precipitable water vapor content in Egypt," *Egyptian J. Remote Sens. Space Sci.*, vol. 19, no. 2, pp. 333–342, Dec. 2016.

[4] L. Yang, Y. Fu, J. Zhu, Y. Shen, and C. Rizos, "Overbounding residual zenith tropospheric delays to enhance GNSS integrity monitoring," *GPS Solutions*, vol. 27, no. 2, p. 76, Apr. 2023.

[5] G. Fotopoulos and M. E. Cannon, "An overview of multi-reference station methods for cm-level positioning," *GPS Solutions*, vol. 4, no. 3, pp. 1–10, Jan. 2001.

[6] P. S. de Oliveira et al., "Modeling tropospheric wet delays with dense and sparse network configurations for PPP-RTK," *GPS Solutions*, vol. 21, no. 1, pp. 237–250, Jan. 2017.

[7] A. Wagner, B. Fersch, P. Yuan, T. Rummler, and H. Kunstmann, "Assimilation of GNSS and synoptic data in a convection permitting limited area model: Improvement of simulated tropospheric water vapor content," *Frontiers Earth Sci.*, vol. 10, Apr. 2022, Art. no. 869504.

[8] Q. Zhao, Y. Liu, X. Ma, W. Yao, Y. Yao, and X. Li, "An improved rainfall forecasting model based on GNSS observations," *IEEE Trans. Geosci. Remote Sens.*, vol. 58, no. 7, pp. 4891–4900, Jul. 2020.

[9] H. Li et al., "Detecting heavy rainfall using anomaly-based percentile thresholds of predictors derived from GNSS-PWV," *Atmos. Res.*, vol. 265, Jan. 2022, Art. no. 105912.

[10] J. Liu, X. Chen, J. Sun, and Q. Liu, "An analysis of GPT2/GPT2w+Saastamoinen models for estimating zenith tropospheric delay over Asian area," *Adv. Space Res.*, vol. 59, no. 3, pp. 824–832, Feb. 2017.

[11] Z. W. Li, X. L. Ding, W. Chen, G. X. Liu, Y. K. Shea, and N. Emerson, "Comparative study of empirical tropospheric models for the Hong Kong region," *Surv. Rev.*, vol. 40, no. 310, pp. 328–341, Oct. 2008.

[12] B. Chen and Z. Liu, "A comprehensive evaluation and analysis of the performance of multiple tropospheric models in China region," *IEEE Trans. Geosci. Remote Sens.*, vol. 54, no. 2, pp. 663–678, Feb. 2016.

[13] G. A. McGraw, "Tropospheric error modeling for high integrity airborne GNSS navigation," in *Proc. IEEE/ION Position, Location Navigat. Symp.*, Apr. 2012, pp. 158–166.

[14] W. Ding, X. Chen, W. Chen, F. N. Teferle, and Y. Yuan, "Global zenith wet delay modeling using neural network approach," *GPS Solutions*, vol. 26, no. 1, pp. 1–13, Jun. 2022.

[15] F. Yang, J. Guo, C. Zhang, Y. Li, and J. Li, "A regional zenith tropospheric delay (ZTD) model based on GPT3 and ANN," *Remote Sens.*, vol. 13, no. 5, p. 838, Feb. 2021.

[16] J. Mohammed, "Artificial neural network for predicting global sub-daily tropospheric wet delay," *J. Atmos. Solar-Terrestrial Phys.*, vol. 217, Jun. 2021, Art. no. 105612.

[17] M. O. Selbesoglu, "Prediction of tropospheric wet delay by an artificial neural network model based on meteorological and GNSS data," *Eng. Sci. Technol., Int. J.*, vol. 23, no. 5, pp. 967–972, Oct. 2020.

[18] L. Crocetti et al., "Global, spatially explicit modelling of zenith wet delay with XGBoost," *J. Geodesy*, vol. 98, no. 4, p. 23, Apr. 2024.

[19] Y. Gao, Z. Li, and J. McLellan, "Carrier phase based regional area differential GPS for decimeter-level positioning and navigation," in *Proc. 10th Int. Tech. Meeting Satell. Division Inst. Navigat. (ION GPS)*, 1997, pp. 1305–1313.

[20] G. Wübbena, A. Bagge, G. Seeber, V. Böder, and P. Hankemeier, "Reducing distance dependent errors for real-time precise dgps applications by establishing reference station networks," in *Proc. GPS*, vol. 9, 1996, pp. 1845–1852.

[21] S. Han and C. Rizos, "Instantaneous ambiguity resolution for medium-range GPS kinematic positioning using multiple reference stations," in *International Association of Geodesy Symposia*. Cham, Switzerland: Springer, 1998, pp. 283–288.

[22] L. Dai, S. Han, J. Wang, and C. Rizos, "Comparison of interpolation algorithms in network-based GPS techniques," *Navigation*, vol. 50, no. 4, pp. 277–293, Dec. 2003.

[23] S. Wang, B. Li, Y. Gao, Y. Gao, and H. Guo, "A comprehensive assessment of interpolation methods for regional augmented PPP using reference networks with different scales and terrains," *Measurement*, vol. 150, Jan. 2020, Art. no. 107067.

[24] A. Al-Shaery, S. Lim, and C. Rizos, "Functional models of ordinary Kriging for medium range real-time kinematic positioning based on the virtual reference station technique," in *Proc. 23rd Int. Tech. Meeting Satell. Division The Inst. Navigat. (ION GNSS 2010)*, 2010, pp. 2513–2521.

[25] B.-G. Kim and C. Kee, "Kriging weighting model of network RTK for ground vehicle on rainy day," in *Proc. 13th Asian Control Conf. (ASCC)*, vol. 2, May 2022, pp. 424–428.

[26] R. B. Christianson, R. M. Pollyea, and R. B. Gramacy, "Traditional Kriging versus modern Gaussian processes for large-scale mining data," *Stat. Anal. Data Mining, ASA Data Sci. J.*, vol. 16, no. 5, pp. 488–506, Oct. 2023.

[27] P. Morales-Álvarez, A. Pérez-Suay, R. Molina, and G. Camps-Valls, "Remote sensing image classification with large-scale Gaussian processes," *IEEE Trans. Geosci. Remote Sens.*, vol. 56, no. 2, pp. 1103–1114, Feb. 2018.

[28] E. Schulz, M. Speekenbrink, and A. Krause, "A tutorial on Gaussian process regression: Modelling, exploring, and exploiting functions," *J. Math. Psychol.*, vol. 85, pp. 1–16, Aug. 2018.

[29] V. L. Deringer, A. P. Bartók, N. Bernstein, D. M. Wilkins, M. Ceriotti, and G. Csányi, "Gaussian process regression for materials and molecules," *Chem. Rev.*, vol. 121, no. 16, pp. 10073–10141, Aug. 2021.

[30] A. Sam-Khaniani and R. Naeijian, "Evaluation of modified saastamoinen ZTD model using ground-based GPS observation over Iran," *Earth Sci. Informat.*, vol. 16, no. 3, pp. 2339–2353, Sep. 2023.

[31] U. Vollath, A. Buecherl, H. Landau, C. Pagels, and B. Wagner, "Multi-base rtk positioning using virtual reference stations," in *Proc. 13th Int. Tech. Meeting Satell. Division The Inst. Navigat. (ION GPS 2000)*, 2000, pp. 123–131.

[32] G. Hu, V. Khoo, P. Goh, and C. Law, "Performance of Singapore integrated multiple reference station network (SIMRSN) for RTK positioning," *GPS Solutions*, vol. 6, nos. 1–2, pp. 65–71, Nov. 2002.

[33] C. Xu, H. Wang, L. Ge, C. Yonezawa, and P. Cheng, "InSAR tropospheric delay mitigation by GPS observations: A case study in Tokyo area," *J. Atmos. Solar-Terrestrial Phys.*, vol. 68, no. 6, pp. 629–638, Mar. 2006.

[34] Y. Zheng, Y. Feng, and Z. Bai, "Grid residual tropospheric corrections for improved differential GPS positioning over the Victoria GPS network (GPSnet)," *J. Global Positioning Syst.*, vol. 4, no. 2, pp. 284–290, Dec. 2005.

[35] A. Leick, L. Rapoport, and D. Tatarnikov, *GPS Satellite Surveying*. Hoboken, NJ, USA: Wiley, 2015.

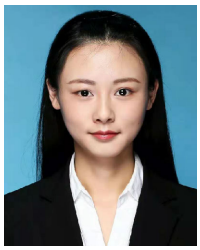

Xuejie Hou received the master's degree in control engineering from the University of Electronic Science and Technology of China, Chengdu, China, in 2021. She is currently pursuing the Ph.D. degree with The Hong Kong Polytechnic University, Hong Kong.

Her research interests include tropospheric modeling and integrity monitoring in Global Navigation Satellite Systems (GNSSs).

Yiping Jiang received the Ph.D. degree from the University of New South Wales, Sydney, NSW, Australia, in 2014.

She is currently an Assistant Professor with the Department of Aeronautical and Aviation Engineering, The Hong Kong Polytechnic University. She lectures on avionics system and satellite navigation for undergraduate and postgraduate students. Her research interests include precise positioning and integrity monitoring for civil aviation and intelligent transportation systems.

Xingqun Zhan (Senior Member, IEEE) received the Ph.D. degree from Harbin Institute of Technology, Harbin, China, in 1999.

He is currently a tenured Professor in navigation and the Associate Dean of Graduate Studies and International Affairs. His research interests include navigation system integrity monitoring, autonomous system cooperative navigation, and Global Navigation Satellite System (GNSS)/inertial/VO integrated navigation.

Dr. Zhan is an AIAA Associate Fellow. He is an Associate Editor of *Aerospace Science and Technology* journal and *Aerospace Systems* journal.